Nuclear Materials and Energy 18 (2019) 326–330

Contents lists available at ScienceDirect

Nuclear Materials and Energy

journal homepage: www.elsevier.com/locate/nme

Properties of fusion-relevant liquid Li-Sn alloys: An *ab initio* molecular-dynamics study

Beatriz G. del Rio[a], Emily K. de Jong[b], Emily A. Carter[c,*]

[a] Department of Mechanical and Aerospace Engineering, Princeton University, Princeton, NJ 08544-5263, USA
[b] Department of Chemical and Biological Engineering, Princeton University, Princeton, NJ 08544-5263, USA
[c] School of Engineering and Applied Science, Princeton University, Princeton, NJ 08544–5263, USA

A B S T R A C T

Plasma-facing conditions in a fusion reactor present challenges of erosion and brittleness for solid materials; a liquid metal alternative potentially could provide a self-healing and replenishing first wall. Among the most promising candidates, Li-Sn alloys have desirable characteristics derived from both of their elemental constituents. However, their deployment has been limited due to a lack of experimental data for many properties at the concentration ratios of interest ($Li_{30}Sn_{70}$ and $Li_{20}Sn_{80}$). Here, we present *ab initio* molecular-dynamics studies of this alloy at both concentration ratios and evaluate relevant properties, including static structure factors and diffusion coefficients of bulk alloys, as well as density profiles and surface segregation of the liquid $Li_{30}Sn_{70}$ film.

1. Introduction

Because of the high temperatures needed to maintain plasmas, future fusion reactors will require thermally robust, durable materials for the inner walls and divertors. Initial approaches employing solids with high melting points [1] presented issues of brittleness and erosion caused by interactions with plasma particles. These limitations may be partly overcome by using liquid metals, which can provide self-replenishing, self-healing plasma-facing surfaces [2]. The most promising candidates so far are lithium (Li) and tin (Sn) due to their low melting points and low evaporation rates. Moreover, the liquid Li-Sn alloy has attracted increasing attention in recent years because it exhibits desirable qualities from each component: the alloy's vapor pressure is much lower than Li's [3] while segregation of Li to the alloy surface [4] reduces pollution of the plasma with high Z atoms (Sn). In addition, deuterium retention in liquid Li-Sn is significantly lower than in pure liquid Li [5]. However, many properties of liquid Li-Sn alloys are still unknown or difficult to measure in both bulk and plasma-facing conditions at fusion-relevant concentrations: $Li_{20}Sn_{80}$ and $Li_{30}Sn_{70}$ [6].

Three studies thus far have quantified some microscopic properties of liquid Li-Sn: laser-induced breakdown spectroscopy determined surface and internal compositions [4]; inelastic neutron scattering (INS) probed bulk liquid structure [7]; and canonical ensemble (constant NVT) Kohn-Sham (KS) density functional theory molecular dynamics (DFT-MD) evaluated structure and diffusion coefficients of a small, bulk sample containing 124 atoms at two different concentrations and temperatures: Li_4Sn at 1040 K and LiSn at 765 K [8]. Here, we perform KSDFT-MD simulations of liquid $Li_{20}Sn_{80}$ and $Li_{30}Sn_{70}$ to elucidate the static structure and dynamics of bulk Li-Sn alloys at Sn-rich concentrations relevant to fusion first walls, and provide the first study of these liquid alloy properties in a thin film configuration. In Section 2, we describe the details of the KSDFT-MD simulations. In Section 3, we give theoretical background for the static and dynamic properties studied. In Section 4, we present our predictions for the static structure and diffusion coefficients of $Li_{20}Sn_{80}$ and $Li_{30}Sn_{70}$, and for surface segregation of Li in liquid $Li_{30}Sn_{70}$, ending with a discussion of some limitations of the computational method.

2. Methodology

2.1. Computational method

We performed MD simulations within the Born-Oppenheimer approximation, where the total energy consists of the sum of the classical ion kinetic energy, the Coulomb repulsion energy between the ions (here “ions” are the positively charged nuclei), and the ground-state energy of the electrons in the presence of the ions. This last term is evaluated within DFT, which expresses the total electronic energy as a functional of the electron density $n(\boldsymbol{r})$ with four distinct contributions

$$E[n(\boldsymbol{r})] = T_s[n(\boldsymbol{r})] + E_{ext}[n(\boldsymbol{r})] + E_H[n(\boldsymbol{r})] + E_{XC}[n(\boldsymbol{r})], \quad (1)$$

where $T_s[n(\boldsymbol{r})]$ is the non-interacting electron kinetic energy, $E_{ext}[n(\boldsymbol{r})]$ is the energy of interaction between the electrons and an external potential (in this case, the ion-electron interaction), $E_H[n(\boldsymbol{r})]$ is the

* Corresponding author.
E-mail address: eac@princeton.edu (E.A. Carter).

https://doi.org/10.1016/j.nme.2019.01.027
Received 27 July 2018; Received in revised form 21 January 2019; Accepted 28 January 2019
Available online 05 February 2019

Hartree electron-electron repulsion energy, and $E_{XC}[n(\boldsymbol{r})]$ is the electron exchange-correlation (XC) energy. We use the projector augmented-wave (PAW) method [9,10] to efficiently perform an all-electron calculation within the frozen-core approximation.

This study employs the KSDFT code VASP [11] to simulate Li_xSn_{1-x} for $x = 0.2$ and $x = 0.3$ at four temperatures: 670, 770, 870, and 970 K. We used the Perdew-Burke-Enzeherhof (PBE) [12] XC functional revised for solids, PBESol [13], for electron XC, as we found that it performs better than PBE or the local density approximation [14,15] in reproducing the atomic density of liquid Sn (*l*-Sn) at 573 K and zero pressure when compared to experimental data [16]. We employed default PAW electron-ion potentials for Li and Sn. Our periodic supercells for $Li_{30}Sn_{70}$ ($Li_{20}Sn_{80}$) contained 360 (500) atoms for both bulk and thin film configurations. We used Methfessel-Paxton [17] Fermi surface smearing with a smearing width of 0.2 eV for all systems. Utilizing a 300 eV kinetic-energy cutoff for the plane-wave basis set ensured convergence of the total energy to within 1 meV/atom. The electron density is expressed using a kinetic-energy cutoff that is four times higher, to achieve sufficient accuracy for MD simulations. The constant NVT KSDFT-MD simulations were performed without k-point sampling. We used the Nosé-Hoover thermostat [18,19] with SMASS = 2, chosen to minimize fluctuations in temperature. We used a time step of 1 fs in all simulations, sufficient to ensure that the total Nosé-Hoover energy quantity is conserved during the entire simulation. After initialization periods of 15 ps, we performed simulations for 40 (20) ps for the bulk (thin film).

2.2. Liquid theory

2.2.1. Static properties

The partial radial distribution function, $g_{ij}(r)$, describes the probability of finding an atom at a distance r from another atom [20].

Coordination tendencies in alloys can be evaluated via the Warren short-range-order (SRO) parameter as generalized by Wagner and Ruppersberg to systems with size effects, α_1 [21]:

$$\alpha_1 = 1 - \frac{n_{ij}}{x_j(x_i(n_{jj} + n_{ji}) + x_j(n_{ii} + n_{ij}))}, \tag{2}$$

where n_{ij} is the number of first-shell neighbors of type j to an atom of type i, $n_{ij} = 4\,\pi\rho\int_0^{R_{ij}} r^2 g_{ij}(r)dr$, with R_{ij} the first minimum in the pair distribution function $G_{ij}(r) = 4\pi r^2 g_{ij}$, and x_i the fraction of atoms of type i. For random distributions $\alpha_1 = 0$, while $\alpha_1 > 0$ and $\alpha_1 < 0$ for homocoordination and heterocoordination, respectively.

The static structure factor, $S(q)$, indicates the presence or absence of order at a certain distance from the origin, measured in reciprocal (q) space and averaged over different spherical directions of q-vectors, *i.e.,* $S(q) = \frac{1}{N}\sum_{j=1}^{N}\sum_{k=1}^{N} e^{-i\vec{q}\cdot\vec{R}_{jk}}$. In a two-component alloy, $S(q)$ can be computed for the homotypic and heterotypic interactions leading to the Ashcroft-Langreth (AL) partial static structure factors, $S_{ij}(q)$ [22]. From these, one can compute the Bhatia-Thornton (BT) static structure factors [23]: number-number (NN), number-concentration (NC), or concentration-concentration (CC), as

$$S_{NN}(q) = x_1 S_{11}(q) + x_2 S_{22}(q) + 2(x_1x_2)^{1/2} S_{12}(q), \tag{3}$$

$$S_{CC}(q) = x_1x_2\left[x_2 S_{11}(q) + x_1 S_{22}(q) - 2(x_1x_2)^{\frac{1}{2}} S_{12}(q)\right], \tag{4}$$

$$S_{NC}(q) = x_1x_2\left[S_{11}(q) - S_{22}(q) + 2(x_2 - x_1)S_{12}(q)/(x_1x_2)^{\frac{1}{2}}\right]. \tag{5}$$

$S_{CC}(q)$ describes the relative arrangement of different species. $S_{CC}(q \to 0) = x_1x_2$ for an ideal alloy at large distances, $S_{CC}(q \to 0) \gg x_1x_2$ for homocoordinating systems, and $S_{CC}(q \to 0) < x_1x_2$ for heterocoordinating systems.

The total neutron-weighted static structure factor $S_{tot}(q)$ is evaluated from the AL $S_{ij}(q)$ [24],

$$\langle b^2\rangle S_{tot}(q) = \sum_{i=1}^{2}(\langle b_i^2\rangle - \langle b_i\rangle^2)x_i + \sum_{i,j=1}^{2}(x_ix_j)^{\frac{1}{2}}\langle b_i\rangle\langle b_j\rangle S_{ij}(q), \tag{6}$$

where $\langle b_i\rangle$ is the coherent scattering length for each atom of type i, and $\langle b^2\rangle = \sum_{i=1}^{2} x_i\langle b_i^2\rangle$ is the average scattering cross-section.

2.2.2. Single-particle dynamics

The self-diffusion coefficient D_i^s can be obtained in two ways. First, from the slope of the mean-squared displacement (MSD), $\langle R^2\rangle = \frac{1}{N}\sum_{j=1}^{N}(\vec{R}_j(t) - \vec{R}_j(0))^2$, of a tagged particle in the liquid [20] as a function of time, $\lim_{t\to\infty}\langle R^2\rangle = 6D_i^s t$. Second, from the tagged particle's velocity-autocorrelation function (VACF), $Z_i^s(t) = \frac{1}{3}\langle\vec{v}_i(t)\cdot\vec{v}_i(0)\rangle$, where $\vec{v}_i(t)$ is the velocity vector. It can be shown [20] that $D_i^s = \int_0^\infty Z_i^s(t)dt$. We evaluated the MSD (VACF) by averaging over 2.8 (1) ps trajectories sampled every 5 (1) fs from the full 40 ps simulation.

In a two-component alloy, the mobility and coupling between the velocities of the particles can be obtained from the time-correlation functions among the atomic velocities. The relative VACF of the center-of-mass of species i in species j is defined as [25]

$$Z_{ij}(t) = \frac{1}{3}x_ix_jN\langle(\vec{v}_i(t) - \vec{v}_j(t))^T(\vec{v}_i(0) - \vec{v}_j(0))\rangle, \tag{7}$$

where $v_j(t)$ is the average velocity of component j. This relative VACF is expressed in terms of self, Z_{ij}^0, and distinct, Z_{ij}^d, components

$$Z_{ij}(t) = (1 - \delta_{ij})Z_{ij}^0(t) + x_ix_jZ_{ij}^d(t), \tag{8}$$

with $Z_{ij}^0(t) = x_iZ_i^s(t) + x_jZ_j^s(t)$. With this formalism, the respective time integrals yield

$$D_{ij} = D_{ij}^0 + x_ix_jD_{ij}^d = D_{ij}^0(1 + \gamma_{ij}), \tag{9}$$

where the coefficient γ_{ij} describes deviations from non-ideal mixtures ($\gamma_{ij} = 0$ for an ideal mixture).

2.2.3. Liquid film

For a free-standing film, the average ion density profile (DP) is a histogram representation of the number of atoms of type i in the direction normal to the film, which in our case is the z-axis. For a metallic liquid film, this measure yields oscillations that are largest at the surfaces of the film and that diminish at the center of the film. However, the presence of thermally induced capillary waves (CWs) may blur such a profile, complicating its analysis. In this work, we employ a method proposed by Chacón and Tarazona (CT) [26] to eliminate such CWs and obtain the average intrinsic density profile (IDP) by referencing the atomic distances to a calculated liquid-vapor separation surface, $z = \xi(x, y)$, at each time step: $z_{i,rel} = z_i - \xi(x_i, y_i)$, where i represents one atom in the sample.

3. Results and discussion

We start by computing the atomic density of each desired concentration at each temperature. As neither $Li_{30}Sn_{70}$ nor $Li_{20}Sn_{80}$ exhibit a stable crystalline structure, we modified the Li_2Sn_5 crystalline structure by subtracting either Li or Sn atoms to obtain the desired concentration of each species, and then performed constant NVT-MD simulations at 1500 K for 3 ps to achieve disorder. After this initial thermalization, we calculated the atomic density at each temperature using the process described by Chen et al. [27], of performing a linear extrapolation/interpolation to zero pressure starting from two initial atomic densities: a weighted average of the experimental densities of Sn and Li and another, 5% higher.

As can be observed in Fig. 1, the density obtained from KSDFT-MD agrees very well with available experimental data [28], which indicates a correct representation of the system.

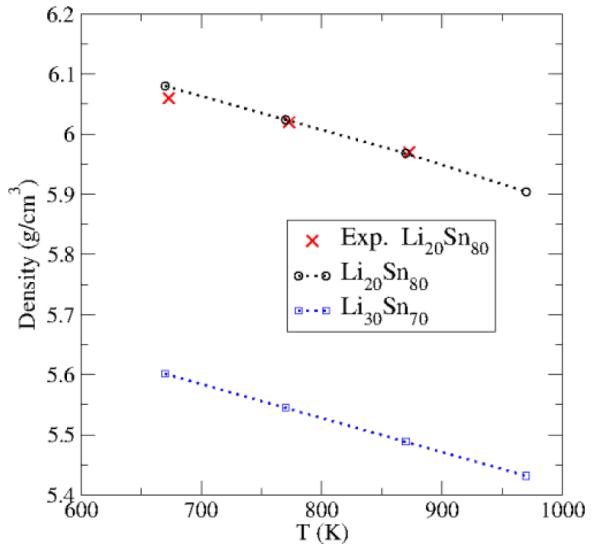

Fig. 1. KSDFT-MD calculated density at 0 GPa for $Li_{20}Sn_{80}$ and $Li_{30}Sn_{70}$. $Li_{20}Sn_{80}$, with experimental data from Kang and Terai [28].

3.1. Static structure

Fig. 2 displays $g_{ij}(r)$ for $Li_{30}Sn_{70}$ (left) and $Li_{20}Sn_{80}$ (right). The first peak in $g_{LiSn}(r)$ occurs at a smaller r than in $g_{LiLi}(r)$ or $g_{SnSn}(r)$, indicating that the distance between a Li and Sn neighbor is smaller than between two Li neighbors or two Sn neighbors. Table 1 displays the coordination numbers and short-range order parameters for the alloy: that the SRO parameters are negative for every concentration and temperature indicates a heterocoordinating alloy. This heterocoordination tendency also explains the slightly larger separation between peaks of the self $g_{ii}(r)$ for both alloys than for the pure liquid metals [16,29] as determined by ND, indicating a larger separation between like atoms in the alloy.

The total static structure factor (Fig. 3) is in good accord with the INS data of Alblas et al. for a $Li_{34.5}Sn_{65.5}$ alloy at a similar temperature [7]. The location of the first peak of $S_{tot}(q)$ matches the experimental

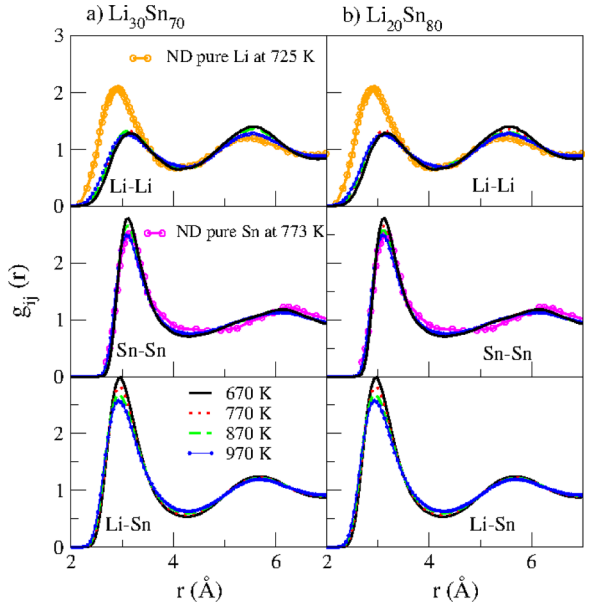

Fig. 2. $g_{ij}(r)$ from KSDFT-MD data for liquid a) $Li_{30}Sn_{70}$ and b) $Li_{20}Sn_{80}$ at four temperatures: 670 K (solid black), 770 K (dotted red), 870 K (dashed green), and 970 K (circle-dotted blue). Experimental neutron diffraction (ND) data for pure liquid Li [29] (orange) and pure liquid Sn [30] (pink).

Table 1
Number of first-shell neighbors and the Wagner SRO parameter for $Li_{30}Sn_{70}$ (black) and for $Li_{20}Sn_{80}$ (bold red).

T (K)	n_{LiLi}	n_{LiSn}	n_{SnLi}	n_{SnSn}	α_1
670	2.4/**1.4**	8.7/**10.1**	3.7/**2.5**	7.1/**9.3**	−0.13/−**0.09**
770	2.4/**1.5**	8.7/**9.9**	3.7/**2.5**	7.1/**9.0**	−0.13/−**0.08**
870	2.4/**1.4**	8.5/**9.8**	3.7/**2.5**	7.2/**9.0**	−0.10/−**0.08**
970	2.3/**1.4**	8.4/**9.1**	3.6/**2.3**	6.9/**8.1**	−0.12/−**0.09**

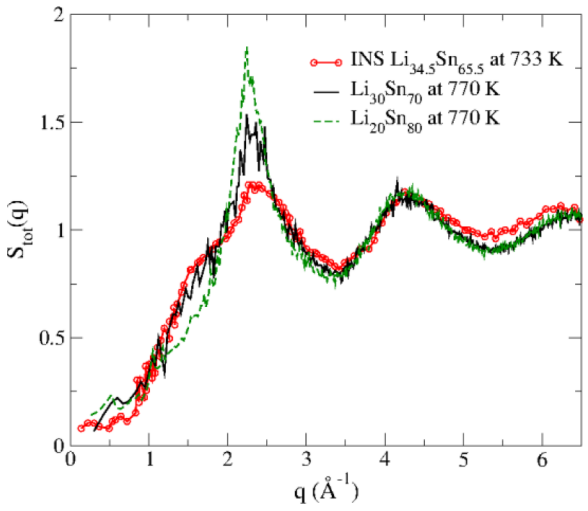

Fig. 3. $S_{tot}(q)$ at 770 K of $Li_{30}Sn_{70}$ (black solid) and $Li_{20}Sn_{80}$ (green dashed), and INS data for $Li_{34.5}Sn_{65.5}$ at 733 K [7] (red circles).

data, indicating a correct representation of the overall structure of the system, yet we do not recover the height of the peak. However, given that the peak height decreases with increasing Li concentration between the two KSDFT-MD model alloys, it seems reasonable to assume that a computational study at the same concentration used by Alblas et al. would recover the experimental peak height. At larger concentrations of Li, $S_{tot}(q)$ shows a shoulder prior to the main peak, also present in the experimental data, which disappears in $Li_{20}Sn_{80}$, indicating a small amount of intermediate order at larger distances.

The AL $S_{LiLi}(q)$ (Fig. 4(a)) exhibits an additional pre-peak, indicating the presence of some long-range ordering not found in pure liquid Li. The experimental data for $S_{NN}(q)$ is not directly measured, but rather derived from a postulated relationship to $S_{tot}(q)$; thus, any discrepancy in the location of the first peak between our KSDFT-MD data and the experimental data could be partly due to an error in this mathematical relationship [7]. Moreover, there is no peak in $S_{CC}(q)$ (Fig. 4(b)) corresponding to the pre-peak from $S_{LiLi}(q)$, and thus this pre-peak probably is not induced by chemical ordering. Finally, $S_{CC}(q)$ at both concentrations decays rapidly at low q, $S_{CC}(q \to 0) < x_1 x_2$, therefore the alloy tends to form pairs of unlike atoms rather than like atoms, indicating heterocoordination.

3.2. Diffusion coefficients

Fig. 5 displays the evaluated self-diffusion coefficients from the MSD and the self-VACF. While 0.8 ps is sufficient for the self-VACF to decay to zero, the VACF for the center-of-mass (Eq. (8)) shows oscillations that persist over long times, introducing significant uncertainty into the calculation, as reflected by the large error bars.

Although no experimental data for this alloy are available for comparison, the predicted Sn self-diffusion coefficients are more similar to *l*-Sn experimental data than those of *l*-Li ($D^s_{Li,pure\ 670K} = 1.65$ Å$^2/ps$) [32]. The decrease in the Li self-diffusion coefficients in the alloy presumably is due to collisions of Li atoms with the much heavier Sn

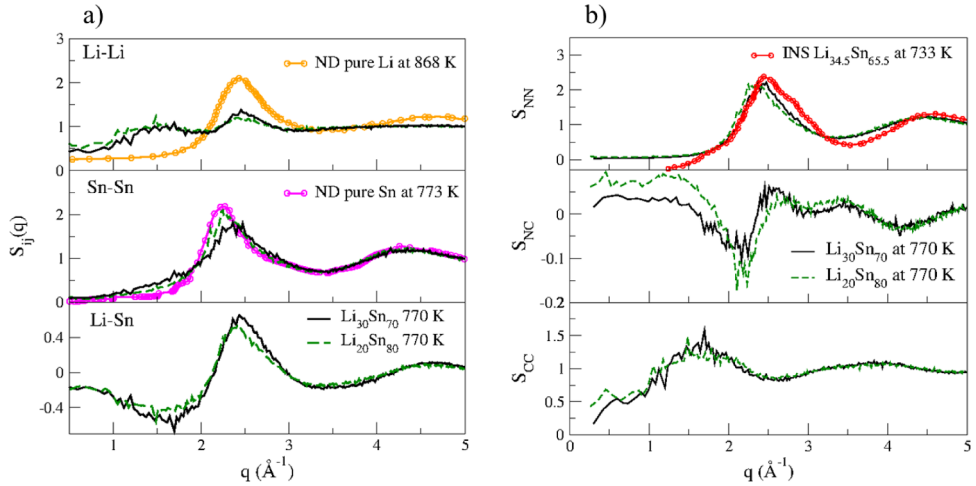

Fig. 4. a) AL $S_{ij}(q)$, at 770 K of $Li_{30}Sn_{70}$ (black solid) and $Li_{20}Sn_{80}$ (green dashed), and ND data for pure Li at 868 K [29] (orange circles) and pure Sn at 773 K [30] (pink circles); b) BT static structure factors at 770 K of $Li_{30}Sn_{70}$ (black solid) and $Li_{20}Sn_{80}$ (green dashed), and INS data for $Li_{34.5}Sn_{65.5}$ at 733 K [7] (red circles).

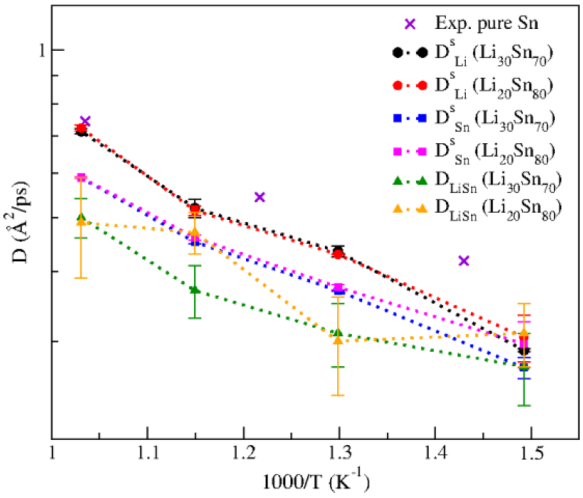

Fig. 5. Self-diffusion coefficients of Li (circles) and Sn (squares), along with overall diffusion coefficients of the alloys (triangles) at different temperatures. Pure *l*-Sn experimental diffusion coefficients by Bruson and Gerl [31] are shown as crosses.

atoms. As anticipated, D_i^s increases with temperature but shows a less-clear trend for D_{LiSn}, likely due to the uncertainty introduced by the oscillations at long times in the VACF.

3.3. Liquid $Li_{30}Sn_{70}$ film. Intrinsic density profile

For the free-standing liquid films, we started from a bulk parallelepiped supercell with the pre-computed bulk ion density at each temperature using the same number of atoms as in the bulk simulations. We disordered each system by performing KSDFT-MD at constant volume for 2 ps at 1500 K and then thermalizing it for an additional 2 ps at the desired temperature. We then added 10 Å of vacuum on each side of the z-direction of the supercell to create a liquid slab (thus, each slab is separated 20 Å from each other). As *l*-Li has a lower surface tension than *l*-Sn [33], Li atoms should segregate and concentrate at the surface to lower the total energy of the film. However, none of the liquid films exhibited any meaningful segregation after more than 40 ps, meaning that this process is too slow for KSDFT-MD. We therefore generated four slab configurations with different initial amounts of Li segregation at the surface by displacing Li atoms with a certain probability (20, 40, 60 and 80%) from the interior of the film (central half) to either one of the two surface regions, and Sn atoms from the surface regions to the interior of the slab. The displacement is such that the initial distance of each Li(Sn) atom to the center(surface) of the film is afterwards its distance to the surface(center). Each initial configuration was first simulated at 1500 K for 2 ps to restore disorder and then thermalized at 670 K for 5 ps. The total energy from the last 2 ps was collected from the simulations; we thus found that a concentration of 49% Li at the surface (derived from the initial segregation with a 60% probability) exhibited the lowest energy at 670 K. We subsequently took this specific configuration and thermalized it at each of the four temperatures of interest for 5 ps until the total Nosé-Hoover energy was constant. Afterward, we simulated another 15 ps to obtain the necessary data for calculation of the ion DP. The decision to start at each temperature from the same initial segregation as the one at 670 K does not introduce meaningful errors, as 20 ps of time is sufficient for the system to equilibrate. Especially in the two systems under study, experimental results confirm that the concentration of Li at the surface does not vary significantly in the range of temperatures studied [34].

As anticipated from its lower surface energy, Li in the $Li_{30}Sn_{70}$ slab segregates preferentially towards the surface of the slab with a concentration similar to recent measurements of ~ 42 % [4], while Sn remains in the center of the slab (Fig. 6). The amount of Li segregation to the surface at 670 K does not vary significantly as temperature increases up to 970 K (not shown). However, due to the small system size, the segregation of Li to the surfaces causes the effective concentration inside the slab to be closer to 20% than 30%. Unfortunately, KSDFT-MD is too costly to represent larger systems with vacuum. A solution for future work is to use orbital-free (OF)DFT [35–37], which, by eliminating the use of orbitals, allows for the study of a much larger system for longer times at the sacrifice of some accuracy. Future comparison between existing KSDFT and future OFDFT data will assess the validity of the representation of the alloys with OFDFT.

4. Conclusions

We simulated two liquid Li-Sn alloys, $Li_{30}Sn_{70}$ and $Li_{20}Sn_{80}$, at four temperatures of interest for plasma-facing applications using KSDFT-MD to study the static and dynamic properties of the bulk liquid and a freestanding liquid film. Clear evidence of heterocoordination with respect to the Li and Sn species is evident from the SRO parameter, α_1, and the behavior of $S_{CC}(q)$ at low q. In addition, $S_{tot}(q)$ and $S_{NN}(q)$ are in good accord with measurements on an alloy close in composition, $Li_{34.5}Sn_{65.5}$.

The self-diffusion coefficients obtained followed the expected trend of increasing D_i^s with increasing temperature. The center-of-mass VACF exhibited large oscillations at longer times, thus introducing a larger

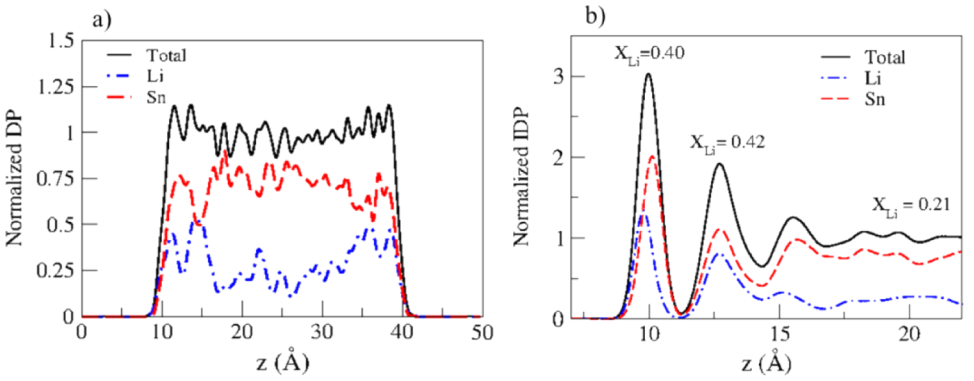

Fig. 6. a) Averaged normalized DP and b) averaged normalized IDP of the $Li_{30}Sn_{70}$ free-standing liquid film from KSDFT-MD at 670 K (black). The ratio of local concentration to average bulk concentration is displayed for Li (dot-dashed blue) and Sn (dashed red) along the film cross-section. X_{Li} represents the concentration of Li in each region of the liquid film.

degree of uncertainty in the calculation of the overall diffusion coefficient, D_{LiSn}, with values lower than any D_i^s, pointing to a small tendency toward compound formation.

For the liquid slab configuration, the ion DP supports the expectation that Li would partition favorably to the surface due to its lower surface tension. Although this tendency was obscured by thermal fluctuations in the form of CWs, the IDP provided clear evidence of segregation. However, the expense of KSDFT-MD limiting both system size and trajectory length introduces significant statistical uncertainty, suggesting that use of properly validated OFDFT-MD might be preferable for future simulation, especially for the freestanding film to reach a more realistic thickness.

Acknowledgments

This work was supported by the Office of Naval Research (Grant no. N00014-15-1-2218) to E.A.C. The authors thank the Computational Science and Engineering Support (CSES) group at Princeton University for maintaining the Terascale Infrastructure for Groundbreaking Research in Science and Engineering (TIGRESS). The authors are indebted to Ms. Nari Baughman for careful editing and Mr. William C. Witt for critical reading of this manuscript.

References

[1] J.P.S. Loureiro, F.L. Tabarés, H. Fernandes, C. Silva, R. Gomes, E. Alves, R. Mateus, T. Pereira, H. Alves, H. Figueiredo, Behavior of liquid Li-Sn alloy as plasma facing material on ISTTOK, Fusion Eng. Des. 117 (2017) 208–211, https://doi.org/10.1016/j.fusengdes.2016.12.031.

[2] J.W. Coenen, G. De Temmerman, G. Federici, V. Philipps, G. Sergienko, G. Strohmayer, A. Terra, B. Unterberg, T. Wegener, D.C.M. Van den Bekerom, Liquid metals as alternative solution for the power exhaust of future fusion devices: status and perspective, Phys. Scr. T159 (2014) 014037, , https://doi.org/10.1088/0031-8949/2014/t159/014037.

[3] R.F. Mattas, J.P. Allain, R. Bastasz, J.N. Brooks, T. Evans, A. Hassanein, S. Luckhardt, K. McCarthy, P. Mioduszewski, R. Maingi, E. Mogahed, R. Moir, S. Molokov, N. Morely, R. Nygren, T. Rognlien, C. Reed, D. Ruzic, I. Sviatoslavsky, D. Sze, M. Tillack, M. Ulrickson, P.M. Wade, R. Wooley, C. Wong, ALPS-Advanced Limiter-divertor Plasma-facing Systems, Fusion Eng. Des. 49–50 (2000) 127–134.

[4] M. Suchonová, J. Kristof, M. Pribula, M. Veis, F.L. Tabarés, P. Veis, Analysis of LiSn alloy at several depths using LIBS, Fusion Eng. Des. 117 (2017) 175–179, https://doi.org/10.1016/j.fusengdes.2016.08.010.

[5] J.P.S. Loureiro, H. Fernandes, F.L. Tabarés, G. Mazzitelli, C. Silva, R. Gomes, E. Alves, R. Mateus, T. Pereira, H. Figueiredo, H. Alves, Deuterium retention in tin (Sn) and lithium–tin (Li–Sn) samples exposed to ISTTOK plasmas, Nucl. Mater. Energy 12 (2017) 709–713, https://doi.org/10.1016/j.nme.2016.12.026.

[6] J.P. Allain, D.N. Ruzic, M.R. Hendricks, D, He and Li sputtering of liquid eutectic Sn–Li, J. Nucl. Mater. 290–293 (2001) 33–37, https://doi.org/10.1016/S0022-3115(00)00504-3.

[7] B.P. Alblas, W. van der Lugt, J. Dijkstra, C. van Dijk, Structure of liquid Li-Sn alloys, J. Phys. F Met. Phys. 14 (1984) 1995–2006, https://doi.org/10.1088/0305-4608/14/9/006.

[8] O. Genser, J. Hafner, Structure and bonding in crystalline and molten Li-Sn alloys: a first-principles density-functional study, Phys. Rev. B 63 (2001) 144204, , https://doi.org/10.1103/PhysRevB.63.144204.

[9] P.E. Blöchl, Projector augmented-wave method, Phys. Rev. B 50 (1994) 17953–17979, https://doi.org/10.1103/PhysRevB.50.17953.

[10] G. Kresse, D. Joubert, From ultrasoft pseudopotentials to the projector augmented-wave method, Phys. Rev. B 59 (1999) 1758–1775, https://doi.org/10.1103/PhysRevB.59.1758.

[11] G. Kresse, J. Furthmüller, Efficient iterative schemes for ab initio total-energy calculations using a plane-wave basis set, Phys. Rev. B 54 (1996) 11169–11186, https://doi.org/10.1103/PhysRevB.54.11169.

[12] J.P. Perdew, K. Burke, M. Ernzerhof, Generalized gradient approximation made simple, Phys. Rev. Lett. 77 (1996) 3865–3868, https://doi.org/10.1103/PhysRevLett.77.3865.

[13] J.P. Perdew, A. Ruzsinszky, G.I. Csonka, O.A. Vydrov, G.E. Scuseria, L.A. Constantin, X. Zhou, K. Burke, Restoring the density-gradient expansion for exchange in solids and surfaces, Phys. Rev. Lett. 100 (2008) 136406, , https://doi.org/10.1103/PhysRevLett.100.136406.

[14] D.M. Ceperley, B.J. Alder, Ground state of the electron gas by a stochastic method, Phys. Rev. Lett. 45 (1980) 566–569, https://doi.org/10.1103/PhysRevLett.45.566.

[15] J.P. Perdew, A. Zunger, Self-interaction correction to density-functional approximations for many-electron systems, Phys. Rev. B 23 (1981) 5048–5079, https://doi.org/10.1103/PhysRevB.23.5048.

[16] Y. Waseda, The Structure of Non-Crystalline Materials: Liquids and Amorphous Solids, McGraw Hill International Book Co., New York, 1980.

[17] M. Methfessel, A.T. Paxton, High-precision sampling for Brillouin-zone integration in metals, Phys. Rev. B 40 (1989) 3616–3621, https://doi.org/10.1103/PhysRevB.40.3616.

[18] S. Nosé, A unified formulation of the constant temperature molecular dynamics methods, J. Chem. Phys. 81 (1984) 511–519, https://doi.org/10.1063/1.447334.

[19] W.G. Hoover, Canonical dynamics: equilibrium phase-space distributions, Phys. Rev. A 31 (1985) 1695–1697, https://doi.org/10.1103/PhysRevA.31.1695.

[20] U. Balucani, M. Zoppi, Dynamics of the Liquid State, Clarendon Press, Oxford, 1994.

[21] C.N.J. Wagner, H. Ruppersberg, Neutron and X-ray diffraction studies of the structure metallic classes, At. Energy Rev. (1981) 1.

[22] N.W. Ashcroft, D.C. Langreth, Structure of binary liquid mixtures. I, Phys. Rev. 156 (1967) 685–692, https://doi.org/10.1103/PhysRev.156.685.

[23] J.P. Boon, S. Yip, Molecular Hydrodynamics, McGraw Hill, Dover, 1980.

[24] G.E. Bacon, Neutron Diffraction, Third ed., Claredon Press, Oxford, 1975.

[25] J. Trullàs, J.A. Padró, Diffusion in multicomponent liquids: a new set of collective velocity correlation functions and diffusion coefficients, J. Chem. Phys. 99 (1993) 3983–3989, https://doi.org/10.1063/1.466191.

[26] E. Chacón, P. Tarazona, Intrinsic profiles beyond the capillary wave theory: a monte carlo study, Phys. Rev. Lett. 91 (2003) 166103, , https://doi.org/10.1103/PhysRevLett.91.166103.

[27] M. Chen, T. Abrams, M.A. Jaworski, E.A. Carter, Rock-salt structure lithium deuteride formation in liquid lithium with high-concentrations of deuterium: a first-principles molecular dynamics study, Nucl. Fusion 56 (2016) 016020, , https://doi.org/10.1088/0029-5515/56/1/016020.

[28] Y. Kang, T. Terai, Hydrogen isotope behaviors in lithium-tin alloy as a potential liquid breeder or coolant for fusion reactor, 2004.

[29] P.S. Salmon, I. Petri, P.H.K. de Jong, P. Verkerk, H.E. Fischer, W.S. Howells, Structure of liquid lithium, J. Phys. Condens. Matter. 16 (2004) 195, https://doi.org/10.1088/0953-8984/16/3/002.

[30] T. Itami, S. Munejiri, T. Masaki, H. Aoki, Y. Ishii, T. Kamiyama, Y. Senda, F. Shimojo, K. Hoshino, Structure of liquid Sn over a wide temperature range from neutron scattering experiments and first-principles molecular dynamics simulation: a comparison to liquid Pb, Phys. Rev. B 67 (2003) 064201, , https://doi.org/10.1103/PhysRevB.67.064201.

[31] A. Bruson, M. Gerl, Diffusion Coefficient of 113 Sn, 124 Sb, 110 m Ag, and 195 Au in Liquid Sn, Phys. Rev. B 21 (1980) 5447–5454.

[32] N.M. Blagoveshchenskii, A.G. Novikov, V.V. Savostin, Self-diffusion in liquid lithium from coherent quasielastic neutron scattering, Phys. B 407 (2012) 4567–4569, https://doi.org/10.1016/j.physb.2012.07.027.

[33] K.A. Yakimovich, A.G. Mozgovoi, Experimental investigation of the density and surface tension of molten lithium at temperatures up to 1300 K, High Temp. 38 (2000) 657–659.

[34] B.B. Alchagirov, R.K. Arkhestov, F.F. Dyshekova, Electron work function in alloys with alkali metals, Tech. Phys. 57 (2012) 1541–1546, https://doi.org/10.1134/S1063784212110023.

[35] P. Hohenberg, W. Kohn, Inhomogeneous electron gas, Phys. Rev. 136 (1964) B864–B871, https://doi.org/10.1103/PhysRevB.7.1912.

[36] Y.A. Wang, E.A. Carter, Orbital-free kinetic-energy density functional theory, in: S.D. Schwartz (Ed.), Theoretical Methods in Condensed Phase Chemistry, Springer, Dordrecht, 2002: pp. 117–184.

[37] W.C. Witt, B.G. del Rio, J.M. Dieterich, E.A. Carter, Orbital-free density functional theory for materials research, J. Mater. Res. 33 (2018) 777–795, https://doi.org/10.1557/jmr.2017.462.